

Effect of the Electron Transport Layer Thickness on $I-V$ Characteristics of the S-Shaped Kinks in Perovskite Solar Cells

Jingxian Liu^{ID}, Bohao Yu, Kaoming Chen^{ID}, Wanling Deng^{ID}, Yuzhao Yang, and Junkai Huang^{ID}

Abstract—In our experimental preparation of perovskite solar cells (PSCs), when the thickness of the electron transport layer (ETL) was changed from thin to thick, the current–voltage ($I-V$) characteristics showed the changing laws of S-shaped kinks appearance, S-shaped kinks disappearance, and S-shaped kinks appearance. A lumped-parameter equivalent circuit model is proposed to reveal the intrinsic physical significances of the S-shaped kinks for this variation laws. The explicit solution of the model is derived using the deformed difference-microvariation (DM) principle combined with the region method, and the model parameters are extracted efficiently through the firefly optimization algorithm (FA). The proposed analytical solution enables the model to be compactly implemented in photovoltaic devices and circuit simulators, and the model is expected to point the direction for process optimization of devices.

Index Terms—Circuit model, electron transport layer (ETL), parameter extraction, S-shaped $I-V$ characteristics.

I. INTRODUCTION

TO DEAL with the energy crisis, it is imperative to research clean and sustainable new energy. Solar energy, a sustainable power source, has received significant attention from researchers. The perovskite solar cells (PSCs) with excellent performance have become a research hot spot [1], [2], [3]. Nevertheless, the anomalous S-shaped kinks observed in the current–voltage ($I-V$) curves with electron transport layer (ETL) changes reduce power conversion efficiency (PCE) [4], [5], which becomes an urgent problem

Manuscript received 14 December 2022; revised 6 February 2023; accepted 7 February 2023. Date of publication 22 February 2023; date of current version 24 March 2023. This work was supported by the Guangdong Natural Science Foundation under Grant 2020A1515010567. The review of this article was arranged by Editor H. Nguyen. (Corresponding author: Junkai Huang.)

Jingxian Liu, Bohao Yu, Kaoming Chen, Wanling Deng, and Junkai Huang are with the Key Laboratory of New Semiconductors and Devices of Guangdong Higher Education Institutes, Department of Electronic Engineering, Jinan University, Guangzhou 510630, China (e-mail: dwanl@126.com; hjk196310@126.com).

Yuzhao Yang is with the School of Chemical Engineering and Light Industry, Guangdong University of Technology, Guangzhou 510006, China, and also with the Department of Electronic Engineering, Jinan University, Guangzhou 510630, China (e-mail: yangyuzh@gdut.edu.cn).

Color versions of one or more figures in this article are available at <https://doi.org/10.1109/TED.2023.3245050>.

Digital Object Identifier 10.1109/TED.2023.3245050

of high-performance PSCs' development. The research on this anomaly revealed that the appearance of S-shaped kinks is caused by charge accumulation [6], interface effect [7], or trap states [8]. However, the S-shaped kinks due to ETL changes have not been accurately described. Therefore, developing a lumped-parameter equivalent circuit model that can completely simulate the S-shaped kinks varying with ETL thickness and visualize the physical properties inside the device is necessary.

Specifically, there are various lumped-parameter equivalent circuit models for simulating and analyzing the $I-V$ characteristics of solar cells [9]. At the circuit topology level, the single-diode model [10] is the most concise representation of the $I-V$ characteristics of solar cells, and it only can realize J-shaped $I-V$ curves. The multidiode models [7], [11], [12], [13], [14], [15], [16] with more complex circuit structures can describe normal and deformed $I-V$ curves. The series multidiode models [7], [11], [12], [13] add an auxiliary circuit into the single-diode model to explain the kinks. However, the model [7] cannot accurately describe the $I-V$ characteristics under high forward voltage, and these models cannot obtain the explicit solution of terminal current due to the complex circuit topology [11], [12], [13].

The model proposed by Mazhari [14] and Xu et al. [17] is considered the simplest multidiode equivalent circuit model, but the accuracy of simulating the linear rising S-shaped kinks in the third quadrant needs to be improved. Yu et al. [15] improved Mazhari's model, aiming to improve the accuracy of the model and its explicit solution derivation, and did not describe the physical characteristics of the device in depth. The model developed by our group [16] focuses on the construction of analytical solution methods for S-shaped $I-V$ curves and represents the electrical effect of the electrode contact interface. However, this model does not pay attention to the charge accumulation effect at the interface between perovskite and ETL.

ETL's thickness has a great influence on the terminal current of solar cells, and the improper thickness will degrade the battery performance. As the thickness increases, the PCE of photovoltaic devices shows a change that gradually increases and then decreases [18], [19]. It should be pointed out that the analysis of S-shaped kinks with ETL changes is still in

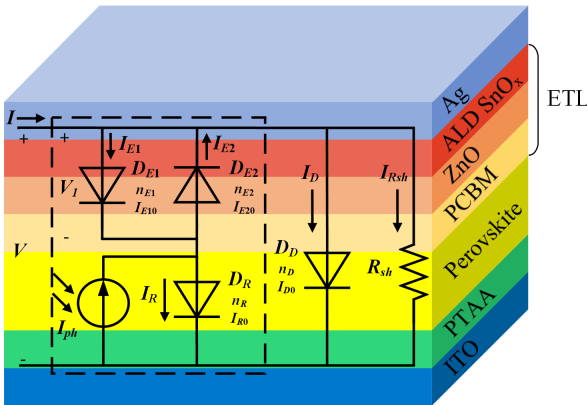


Fig. 1. Lumped parameters equivalent circuit model of PSCs.

the experimental and mechanism analysis [20], [21], [22], and a circuit model based on physics has not been used to characterize.

Here, a multidiode circuit model is developed, which includes the diode representing the negative charge accumulation mechanism in the interface. For the PSCs with the structure shown in Fig. 1, the improved model is employed to accurately and systematically characterize the I - V curves under our different ETL thickness processes composed of SnO_x . Moreover, the balance between topology complexity and model accuracy is achieved with as few parameters as possible. In order to solve the problem of parameter extraction difficulty while the accuracy of the model is improved, the intelligent algorithm can be applied to efficiently and accurately extract the parameters of the lumped parameter model. The explicit solution obtained by the deformed difference-microvariation (DM) principle and the region method makes the model compactly applied to photovoltaic devices and circuit simulators.

II. EXPERIMENTAL DETAILS

Different from the device structure in previous work [23], [24], we fabricated PSCs with glass/indium tin oxide (ITO)/poly(triaryl amine) (PTAA)/perovskite/ [6], [6]-phenyl-C61-butyl acid methyl ester (PCBM)/ZnO/SnO_x/Ag. The specific preparation process is as follows. Clean ITO substrate with deionized water, detergent, ethanol, and isopropanol in turn. After plasma treatment for 10 min, spin-coated PTAA (1.5 mg/mL in CB) solution on ITO at 6000 r/min for 30 s and annealed at 120 °C for 10 min. The perovskite precursor solution composed of mixed CsI, FAPbI₃, and MAPbBr₃ was dissolved in mixed solvent (DMF:DMSO = 4:1) with a chemical equation of Cs_{0.05}Fa_{0.83}MA_{0.12}PbI_{2.64}Br_{0.36}. Then, 100- μL precursor solution was spin-coated onto PTAA at 2000 r/min for 10 s and 4000 r/min for 30 s, and wash the films with 240- μL ethyl acetate for 10 s during the second step of spin-coating. The films were annealed at 100 °C for 20 min. After cooling to room temperature, spin-coated PCBM (CB, 15 mg/mL) on top of the perovskite layers at 2000 r/min for 30 s. Then, ZnO solution (2.5 wt% ZnO nanoparticle solution:isopropanol = 1:2 by volume) was spin-coated on

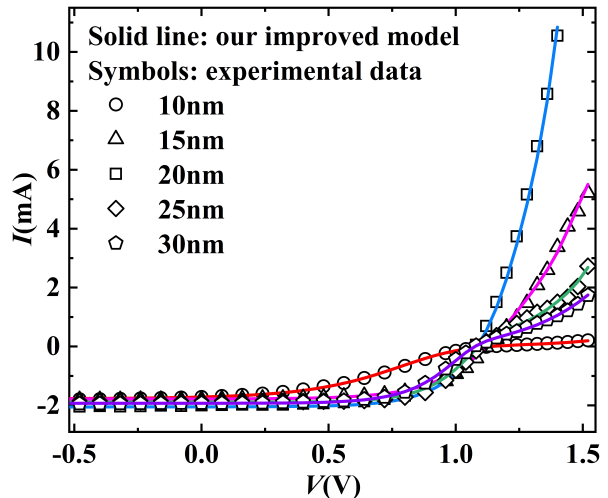


Fig. 2. Comparisons between our model and experimental data.

PCBM at a constant speed of 2000 r/min for 30 s. The films were annealed at 100 °C for about 10 min. In addition, the SnO_x with 100, 150, 200, 250, and 300 cycles was deposited on top of the ZnO in the atomic layer deposition (ALD) reactor (NCE-200R, Dongguan Nanofrontier Microelectronics Equipment Company Ltd.), respectively. The growth rate of ALD SnO_x is 1 Å per cycle. After ALD SnO_x deposition, the device was finished by thermal evaporation of Ag (120 nm) under a vacuum. The prepared solar cell device area is 0.09 cm². The performance measurements of devices without encapsulation were carried out under ambient-air conditions. The current density–voltage (J - V) characteristics of the solar cells were measured using a Keithley 2400. Simulated AM 1.5 G irradiation (100 mW/cm²) was produced by a xenon-lamp-based solar simulator (LIGHTSKY TECH LSS-55, Solar Simulator) for J - V measurements. The light intensity was calibrated by a silicon reference cell (Newport 91150V). The scan speed was fixed at 0.15 V·s⁻¹ and no preconditioning was used in this work. The measured experimental data are the symbols in Fig. 2, and the S-shaped kinks are present at low and high ETL thickness. The photovoltaic parameters of PSCs with different ETL thicknesses are shown in Fig. 3.

III. ANALYTICAL MODEL

To reproduce the S-shaped kinks of PSCs, an improved lumped parameters equivalent circuit model has been proposed, as shown in Fig. 1. It consists of photogenerated current source I_{ph} , four diodes D_R , D_{E1} , D_{E2} , and D_D , and a resistance R_{sh} . I_{ph} is a constant that depends on solar radiation and describes the rate of polaron pair generation. The diode D_R is used to model the losses due to polaron recombination. Diodes D_{E1} and D_{E2} represent the behavior of negative charge accumulation and the extraction of free carriers, respectively. Diode D_D simulates the I - V characteristics of the device under dark conditions. The parallel resistance is applied to characterize the recent loss due to traps and defects in the battery.

The complete circuit topology makes it difficult to derive an explicit solution to the model. To develop a terminal current expression, the following equation can be obtained according to Kirchhoff's current law and Shockley's ideal

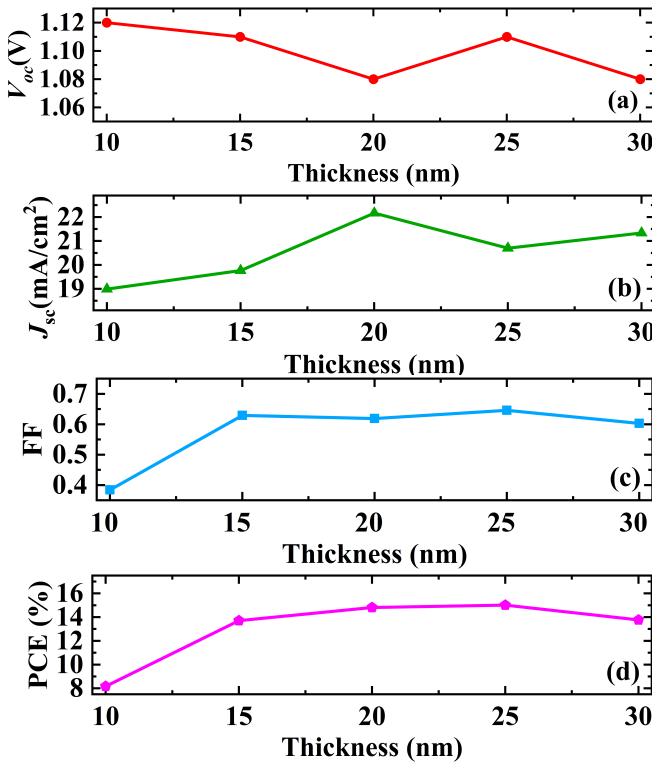


Fig. 3. Photovoltaic parameters of our PSCs with different ETL thicknesses. (a) V_{oc} : open-circuit voltage. (b) J_{sc} : short-circuit current density. (c) FF: fill factor. (d) PCE: power conversion efficiency.

diode current equation [25]:

$$I = I_{E10} \left(e^{\frac{V_1}{n_{E1} V_t}} - 1 \right) - I_{E20} \left(e^{\frac{-V_1}{n_{E2} V_t}} - 1 \right) + I_{D0} \left(e^{\frac{V}{n_D V_t}} - 1 \right) + \frac{V}{R_{sh}} \quad (1)$$

The voltage drop across the diode D_{E1} is V_1 . I_{E10} , I_{E20} , and I_{D0} and n_{E1} , n_{E2} , and n_D are reverse saturation current and ideality factors of the diodes, respectively. The subscripts correspond to the diodes in Fig. 1. V_t is the thermal voltage.

According to the dashed part of the circuit, the influence of diode D_{E1} on the current is incorporated into the following equation as lumped parameters:

$$I_{ph} = I_{R0} \left(e^{\frac{V-V_1}{n_R V_t}} - 1 \right) + I_{E20} \left(e^{\frac{-V_1}{n_{E2} V_t}} - 1 \right) - I_{E10} \left(e^{\frac{V_1}{n_{E1} V_t}} - 1 \right) \quad (2)$$

where I_{R0} and n_R represent the reverse saturation current and ideality factor of the diode D_R , respectively. The analytical solution of node voltage V_1 is difficult to obtain, because the above transcendental equation contains three exponential terms, which cannot be solved directly using the Lambert W function or the DM principle [16]. Therefore, (2) is simplified through the region method [26], [27], [28].

In the operation region of $V_1 > 0$ V, the exponent item of $\exp(-V_1/n_{E2} V_t)$ approaches zero. Rewriting (2), we get

$$I_{ph} = I_{R0} \left(e^{\frac{V-V_1}{n_R V_t}} - 1 \right) - I_{E20} - I_{E10} \left(e^{\frac{V_1}{n_{E1} V_t}} - 1 \right). \quad (3)$$

Equation (3) is also a transcendental function. The common-mode factor and differential-mode factor in DM principle are

used to simplify the calculation process. We can obtain the function as

$$A = I_{R0} e^{\frac{V}{n_R V_t}} e^{\frac{(S_{d1}-S_{c1})V_{1_1}}{V_t}} - I_{E10} e^{\frac{(S_{d1}+S_{c1})V_{1_1}}{V_t}} \quad (4)$$

where $A = I_{ph} + I_{R0} + I_{E20} - I_{E10}$, S_{c1} is the common-mode factor, calculated as $S_{c1} = (1/n_{E1} + 1/n_R)/2$, S_{d1} is the differential-mode factor, and the calculation equation is $S_{d1} = (1/n_{E1} - 1/n_R)/2$. In general, $S_{c1} \gg S_{d1}$, S_{d1} can be ignored, and (4) is mathematically converted to

$$A = I_{R0} e^{\frac{V}{n_R V_t}} e^{-x} - I_{E10} e^x \quad (5)$$

$$I_{E10} t^2 + At - I_{R0} e^{\frac{V}{n_R V_t}} = 0 \quad (6)$$

where $x = (S_{c1} V_{1_1})/V_t$, setting $t = \exp(x)$ ($t > 0$). Solving (6) and we can get the expression of V_{1_1}

$$V_{1_1} = \frac{V_t}{S_{c1}} \ln \left(\frac{-A + \sqrt{\Delta}}{2I_{E10}} \right) \quad (7)$$

where $\Delta = A^2 - 4I_{E10} \times [-I_{R0} \exp(V/(n_R V_t))]$.

In the region where $V_1 < 0$ V, the exponent item of $\exp(V_1/n_{E1} V_t)$ tends to be zero, and (2) can be simplified as

$$I_{ph} = I_{R0} \left(e^{\frac{V-V_1}{n_R V_t}} - 1 \right) + I_{E20} \left(e^{\frac{-V_1}{n_{E2} V_t}} - 1 \right) + I_{E10} \quad (8)$$

$$A = I_{R0} e^{\frac{V}{n_R V_t}} e^{\frac{-(S_{c2}+S_{d2})V_{1_2}}{V_t}} + I_{E20} e^{\frac{-(S_{c2}-S_{d2})V_{1_2}}{V_t}} \quad (9)$$

where $S_{c2} = (1/n_R + 1/n_{E2})/2$ and $S_{d2} = (1/n_R - 1/n_{E2})/2$. After ignoring S_{d2} , an approximate solution for V_{1_2} can be obtained

$$A = I_{R0} e^{\frac{V}{n_R V_t}} e^{\frac{-S_{c2}V_{1_2}}{V_t}} + I_{E20} e^{\frac{-S_{c2}V_{1_2}}{V_t}} \quad (10)$$

$$V_{1_2} = - \left(\frac{V_t}{S_{c2}} \right) \ln \left(\frac{A}{I_{R0} e^{\frac{V}{n_R V_t}} + I_{E20}} \right). \quad (11)$$

As a result, to stitch the various equations into a unified solution which gives an analytical and accurate expression of the node voltage in the entire operation region, a smoothing function is employed to connect V_{1_1} in (7) and V_{1_2} in (11)

$$V_1 = \left[\frac{V_{1_1}}{1 + e^{m_1(x_0-V)}} + \frac{V_{1_2}}{1 + e^{m_1(V-x_0)}} \right] - \omega \quad (12)$$

where m_1 is a weight parameter of 10, and x_0 is the value of V when V_1 is 0 in (2). A correction factor Schroeder series ω [29] is introduced to improve the accuracy of V_1 , $\omega = -(y'/y)/(1 - 0.5yy''/y'^2)$, where $y = I_{R0}[\exp((V-V_1)/n_R V_t) - 1] + I_{E20}[\exp(-V_1/n_{E2} V_t) - 1] - I_{E10}[\exp(V_1/n_{E1} V_t) - 1] - I_{ph}$, and y' and y'' are the first-order and second-order derivatives of y versus V_1 . Finally, substituting (12) into (1), the explicit analytical solution of terminal current can be obtained.

IV. RESULTS AND DISCUSSION

In Fig. 4, the computed results were compared with the iterative results of the Newton-Raphson (NR) method to verify the effectiveness of the V_1 solution method. The errors between NR and our solution could be as low as 10^{-4} V scale, proving the feasibility of our proposed solution for V_1 .

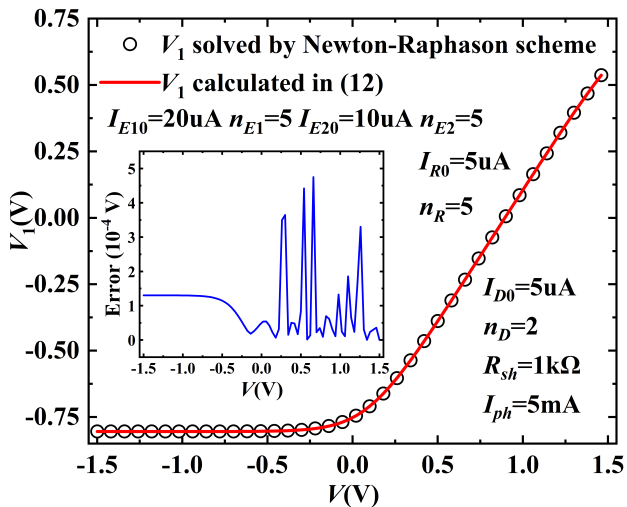


Fig. 4. V_1 solved by NR scheme and calculated in (12). The inset shows the error of V_1 characteristics.

Meanwhile, to accurately and efficiently describe the S-shaped $I-V$ curves of PSCs, a valid parameter extraction routine is required. The parameter extraction routine [30], [31] for the single-diode model is not suitable for the multidiode model, and initial value selection and convergence problems exist in the parameter extraction of the numerical iteration method [32], [33]. Thus, the firefly optimization algorithm (FA) [34], [35] with excellent optimization ability is introduced to extract fitting parameters of the improved model. The extracted parameters are shown in Fig. 5. Each parameter is extracted multiple times, and after removing unreasonable parameters, it is believed that the parameters showing a certain change trend can reflect some intrinsic physical meanings.

In Fig. 2, for the small ETL thickness of 10 nm, the S-shaped kink of the $I-V$ characteristic is exponential-like form. For the medium ETL thickness ranging from 10 to 20 nm, the $I-V$ characteristics show traditional J-shaped curves. For the thick ETL thickness above 20 nm, the $I-V$ characteristics show S-shaped curves with exponential form. In the cases of different ETL thicknesses, our lumped-parameter equivalent circuit model has the ability of accurately simulate the J- and S-shaped curves of PSCs.

Fig. 6 shows the effect of ETL thickness on electronic extraction and transmission in inverted PSCs, which can be used to reveal our experimental results in Figs. 2 and 3 and the physical properties characterized through the lumped parameter equivalent circuit model and parameter extraction in this article.

First, the cell without ETL or very thin ETL, the perovskite layer and the current extraction layer will be in direct contact or fail to form a good interfacial contact, resulting in a large amount of charge recombination. In our model, I_{R0} is the reverse saturation current of the diode D_R that represents the recombination mechanism. It can be seen from Fig. 5(c) that I_{R0} is particularly significant when the thickness of SnO_x in ETL is 10 nm, indicating that the current increases due to the recombination of electrons and holes. As shown in Fig. 3, the photovoltaic device parameters in this case are poor, especially the short-circuit current density (J_{sc}), fill factor (FF), and PCE.

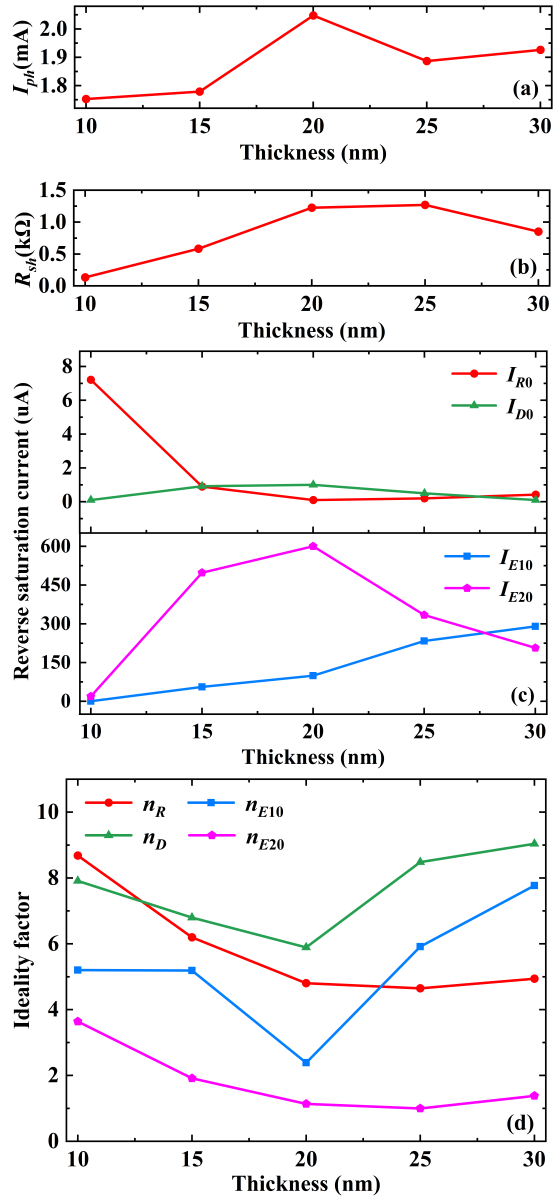


Fig. 5. Model parameters extracted with firefly algorithm. (a) I_{ph} : photocurrent. (b) R_{sh} : parallel resistance. (c) Reverse saturation currents of the diodes. (d) Ideality factors of the diodes.

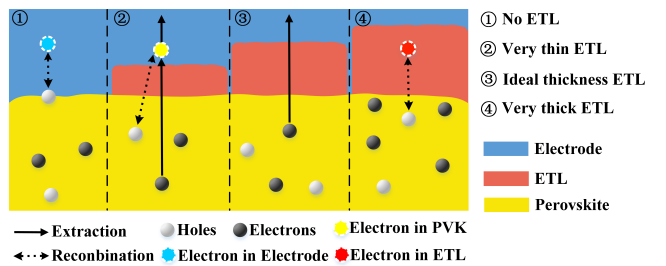


Fig. 6. Schematic of electron transfer and transport mechanism with different ETL thicknesses.

Second, when the thickness of the ETL is appropriate, the ETL promotes effective electron collection and transmission from the perovskite layer to the electrode, and the hole can be blocked to inhibit charge recombination. The diode D_{E2} represents the behavior of the extraction of free carriers in our model. In this case, the large extraction current I_{E20} and small

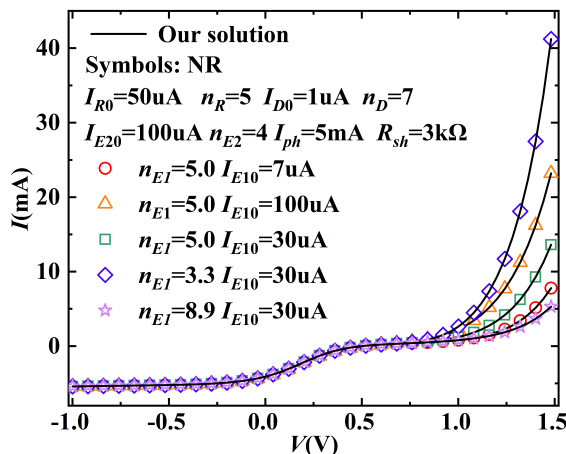


Fig. 7. Effects from I_{E10} and n_{E1} on I - V characteristics of PSCs.

recombination current I_{R0} can be obtained. This is consistent with the result of extracting parameters in Fig. 5(c). The enlarged FF illustrates that the electron extraction mechanism is normal. The PSCs without S-shaped kinks can be achieved, as shown in Fig. 2. Therefore, this is the process range for the optimum thickness of the ETL layer of the perovskite cells.

Third, very thick ETL will lead to increased carrier trap density and significant charge accumulation. In this circumstance, some charges are recombined in the ETL, while others cannot be transferred, which eventually give rise to the generation of the S-shaped kinks, as shown in Fig. 2. The increase of I_{E10} represents the negative charge accumulation behavior, and the decrease of extraction current in Fig. 5(c) also reflects this point. At this time, the photovoltaic parameters, such as FF and PCE, also changed from an upward trend to a downward trend, demonstrating that the battery performance gradually deteriorates.

In fact, in our experimental data, when the thickness of the ETL is relatively large, the kink characteristics in the I - V curves are exponential. Meanwhile, Fig. 7 shows the effect of diode D_{E1} on the I - V curves of PSCs, and our model establishes the exponential S-shaped kinks in the region with large forward terminal voltage. The curvature of S-shaped kinks can be changed through adjusting the parameters of D_{E1} to achieve more detailed regulation. Especially, it has stronger control over the exponential-like and exponential S-shaped I - V curves. The satisfactory fitting between the experimental data indicates the validity of the improved model and the extracted parameters.

V. CONCLUSION

In this article, perovskite photovoltaic devices with different ETL thicknesses were fabricated based on our process. The characteristics of the I - V curves reflect the relevant physical mechanisms of charge generation, extraction, and recombination with different ETL thicknesses. An improved lumped-parameter equivalent circuit model and analytical solution with the deformed DM and region method are developed. This model not only exactly predicts S-shaped kinks with linear, exponential, and exponential-like currents but also reflects the effect of the ETL thickness on the terminal current. The firefly

intelligent algorithm is easy to implement, which is an effective tool for extracting the parameters of the lumped-parameter equivalent circuit model. In addition, the changing trend of model and the parameters can reveal the physical characteristics of the S-shaped kinks of the device, and it is expected to provide direction for optimizing the device process.

REFERENCES

- [1] Z. He, C. Zhong, S. Su, M. Xu, H. Wu, and Y. Cao, "Enhanced power-conversion efficiency in polymer solar cells using an inverted device structure," *Nature Photon.*, vol. 6, pp. 591–595, Jun. 2012, doi: [10.1038/nphoton.2012.190](https://doi.org/10.1038/nphoton.2012.190).
- [2] Q. Jiang et al., "Planar-structure perovskite solar cells with efficiency beyond 21%," *Adv. Mater.*, vol. 29, no. 46, Dec. 2017, Art. no. 1703852, doi: [10.1002/adma.201703852](https://doi.org/10.1002/adma.201703852).
- [3] Z. Lin et al., "Precursor engineering of the electron transport layer for application in high-performance perovskite solar cells," *Adv. Sci.*, vol. 8, no. 22, Oct. 2021, Art. no. 2102845, doi: [10.1002/advs.202102845](https://doi.org/10.1002/advs.202102845).
- [4] S. S. Kim, S. Bae, and W. H. Jo, "Performance enhancement of planar heterojunction perovskite solar cells by n-doping of the electron transporting layer," *Chem. Commun.*, vol. 51, no. 98, pp. 1741–17413, Oct. 2015, doi: [10.1039/C5CC0253J](https://doi.org/10.1039/C5CC0253J).
- [5] K. E. Roelofs et al., "Impact of conformality and crystallinity for ultrathin 4 nm compact TiO₂ layers in perovskite solar cells," *Adv. Mater. Interface*, vol. 3, no. 21, Nov. 2016, Art. no. 1600580, doi: [10.1002/admi.201600580](https://doi.org/10.1002/admi.201600580).
- [6] C. Chen et al., "Effect of BCP buffer layer on eliminating charge accumulation for high performance of inverted perovskite solar cells," *RSC Adv.*, vol. 7, no. 57, pp. 35819–35826, 2017, doi: [10.1039/C7RA06365B](https://doi.org/10.1039/C7RA06365B).
- [7] F. A. D. Castro, J. Heier, F. Nüesch, and R. Hany, "Origin of the kink in current-density versus voltage curves and efficiency enhancement of polymer-C₆₀ heterojunction solar cells," *IEEE J. Sel. Topics Quantum Electron.*, vol. 16, no. 6, pp. 1690–1699, Nov./Dec. 2010, doi: [10.1109/JSTQE.2010.2040807](https://doi.org/10.1109/JSTQE.2010.2040807).
- [8] Y. Shao, Z. Xiao, C. Bi, Y. Yuan, and J. Huang, "Origin and elimination of photocurrent hysteresis by fullerene passivation in CH₃NH₃PbI₃ planar heterojunction solar cells," *Nature Commun.*, vol. 5, no. 1, pp. 1–7, Dec. 2014, doi: [10.1038/ncomms6784](https://doi.org/10.1038/ncomms6784).
- [9] F. García-Sánchez et al., "Modelling solar cell S-shaped I-V characteristics with DC lumped-parameter equivalent circuits a review," *Facta Universitatis Ser. Electron. Energetics*, vol. 30, no. 3, pp. 327–350, 2017, doi: [10.2298/FUEE1703327G](https://doi.org/10.2298/FUEE1703327G).
- [10] V. L. Brano, A. Orioli, G. Ciulla, and A. D. Gangi, "An improved five-parameter model for photovoltaic modules," *Sol. Energy Mater. Sol. Cells*, vol. 94, no. 8, pp. 1358–1370, Aug. 2010, doi: [10.1016/j.solmat.2010.04.003](https://doi.org/10.1016/j.solmat.2010.04.003).
- [11] F. J. García-Sánchez, D. Lugo-Muñoz, J. Muci, and A. Ortiz-Conde, "Lumped parameter modeling of organic solar cells' S-shaped I-V characteristics," *IEEE J. Photovolt.*, vol. 3, no. 1, pp. 330–335, Jan. 2013, doi: [10.1109/JPHOTOV.2012.2219503](https://doi.org/10.1109/JPHOTOV.2012.2219503).
- [12] F. D. Castro, A. Laudani, F. R. Fulginei, and A. Salvini, "An in-depth analysis of the modelling of organic solar cells using multiple-diode circuits," *Sol. Energy*, vol. 135, pp. 590–597, Oct. 2016, doi: [10.1016/j.solener.2016.06.033](https://doi.org/10.1016/j.solener.2016.06.033).
- [13] G. Huang, Y. Liang, X. Sun, C. Xu, and F. Yu, "Analyzing S-shaped I-V characteristics of solar cells by solving three-diode lumped-parameter equivalent circuit model explicitly," *Energy*, vol. 212, Dec. 2020, Art. no. 118702, doi: [10.1016/j.energy.2020.118702](https://doi.org/10.1016/j.energy.2020.118702).
- [14] B. Mazhari, "An improved solar cell circuit model for organic solar cells," *Sol. Energy Mater. Solar Cells*, vol. 90, nos. 7–8, pp. 1021–1033, May 2006, doi: [10.1016/j.solmat.2005.05.017](https://doi.org/10.1016/j.solmat.2005.05.017).
- [15] F. Yu, G. Huang, W. Lin, and C. Xu, "An analysis for S-shaped I-V characteristics of organic solar cells using lumped-parameter equivalent circuit model," *Sol. Energy*, vol. 177, pp. 229–240, Jan. 2019, doi: [10.1016/j.solener.2018.11.011](https://doi.org/10.1016/j.solener.2018.11.011).
- [16] K. Chen et al., "A lumped-parameter equivalent circuit model for perovskite solar cells' S-shaped I-V kinks," *IEEE Electron Device Letters*, vol. 42, no. 3, pp. 379–382, Mar. 2021, doi: [10.1109/LED.2021.3052533](https://doi.org/10.1109/LED.2021.3052533).
- [17] C. Xu, F. Yu, W. Lin, and G. Huang, "An improved organic solar cell lumped-parameter equivalent circuit model," *Crystals*, vol. 8, no. 7, p. 277, Jun. 2018, doi: [10.3390/cryst8070277](https://doi.org/10.3390/cryst8070277).

- [18] P.-Y. Gu et al., "Pushing up the efficiency of planar perovskite solar cells to 18.2% with organic small molecules as the electron transport layer," *J. Mater. Chem. A*, vol. 5, no. 16, pp. 7339–7344, 2017, doi: [10.1039/c7ta01764b](https://doi.org/10.1039/c7ta01764b).
- [19] A. Ślawek, Z. Starowicz, and M. Lipiński, "The influence of the thickness of compact TiO_2 electron transport layer on the performance of planar $CH_3NH_3PbI_3$ perovskite solar cells," *Materials*, vol. 14, no. 12, p. 3295, Jun. 2021, doi: [10.3390/ma14123295](https://doi.org/10.3390/ma14123295).
- [20] J. Choi, S. Song, M. T. Hörantner, H. J. Snaith, and T. Park, "Well-defined nanostructured, single-crystalline TiO_2 electron transport layer for efficient planar perovskite solar cells," *ACS Nano*, vol. 10, no. 6, pp. 6029–6036, May 2016, doi: [10.1021/acsnano.6b01575](https://doi.org/10.1021/acsnano.6b01575).
- [21] T. Wahl, J. Hanisch, S. Meier, M. Schultes, and E. Ahlsweide, "Sputtered indium zinc oxide rear electrodes for inverted semitransparent perovskite solar cells without using a protective buffer layer," *Organic Electron.*, vol. 54, pp. 48–53, Mar. 2018, doi: [10.1016/j.orgel.2017.12.020](https://doi.org/10.1016/j.orgel.2017.12.020).
- [22] F. Li et al., "Effect of $(CH_3)_2Sn(COOH)_2$ electron transport layer thickness on device performance in n-i-p planar heterojunction perovskite solar cells," *J. Phys. Chem. C*, vol. 125, no. 14, pp. 7552–7559, Apr. 2021, doi: [10.1021/acs.jpcc.1c00176](https://doi.org/10.1021/acs.jpcc.1c00176).
- [23] J. Hu et al., "Spontaneously self-assembly of a 2D/3D heterostructure enhances the efficiency and stability in printed perovskite solar cells," *Adv. Energy Mater.*, vol. 10, no. 17, May 2020, Art. no. 2000173, doi: [10.1002/aenm.202000173](https://doi.org/10.1002/aenm.202000173).
- [24] L. Yan et al., "Synergistic passivation of perovskite absorber films for efficient four-terminal perovskite/silicon tandem solar cells," *Adv. Energy Sustainability Res.*, vol. 3, no. 6, Jun. 2022, Art. no. 2100199, doi: [10.1002/aesr.202100199](https://doi.org/10.1002/aesr.202100199).
- [25] W. Shockley, "The theory of p-n junctions in semiconductors and p-n junction transistors," *Bell Syst. Tech. J.*, vol. 28, no. 3, pp. 435–489, Jul. 1949, doi: [10.1002/j.1538-7305.1949.tb03645.x](https://doi.org/10.1002/j.1538-7305.1949.tb03645.x).
- [26] F. Yu, Y. Liang, X. Sun, G. Huang, and C. Xu, "Modelling solar cells' S-shaped I-V characteristics with an analytical solution to lumped-parameter equivalent circuit model," *Sol. Energy*, vol. 202, pp. 498–506, May 2020, doi: [10.1016/j.solener.2020.03.090](https://doi.org/10.1016/j.solener.2020.03.090).
- [27] W. Deng, J. Huang, X. Ma, and T. Ning, "An explicit surface-potential-based model for amorphous IGZO thin-film transistors including both tail and deep states," *IEEE Electron Device Lett.*, vol. 35, no. 1, pp. 78–80, Jan. 2014, doi: [10.1109/LED.2013.2289877](https://doi.org/10.1109/LED.2013.2289877).
- [28] F. Yu, W. Deng, J. Huang, X. Ma, and S. Chen, "An explicit physics-based I-V model for surrounding-gate polysilicon transistors," *IEEE Trans. Electron Devices*, vol. 63, no. 3, pp. 1059–1065, Mar. 2016, doi: [10.1109/TED.2015.2512851](https://doi.org/10.1109/TED.2015.2512851).
- [29] W. Deng and J. Huang, "A physics-based approximation for the polysilicon thin-film transistor surface potential," *IEEE Electron Device Lett.*, vol. 32, no. 5, pp. 647–649, May 2011, doi: [10.1109/LED.2011.211873](https://doi.org/10.1109/LED.2011.211873).
- [30] E. Q. B. Macabebe, C. J. Sheppard, and E. E. van Dyk, "Parameter extraction from I-V characteristics of PV devices," *Sol. Energy*, vol. 85, no. 1, pp. 12–18, Jan. 2011, doi: [10.1016/j.solener.2010.11.005](https://doi.org/10.1016/j.solener.2010.11.005).
- [31] R. Abbassi, A. Abbassi, M. Jemli, and S. Chebbi, "Identification of unknown parameters of solar cell models: A comprehensive overview of available approaches," *Renew. Sustain. Energy Rev.*, vol. 90, pp. 453–474, Jul. 2018, doi: [10.1016/j.rser.2018.03.011](https://doi.org/10.1016/j.rser.2018.03.011).
- [32] I. Nassar-Eddine, A. Obbadi, Y. Errami, A. El Fajri, and M. Agunaou, "Parameter estimation of photovoltaic modules using iterative method and the Lambert w function: A comparative study," *Energy Convers. Manage.*, vol. 119, pp. 37–48, Jul. 2016, doi: [10.1016/j.enconman.2016.04.030](https://doi.org/10.1016/j.enconman.2016.04.030).
- [33] K. Et-Torabi et al., "Parameters estimation of the single and double diode photovoltaic models using a Gauss–Seidel algorithm and analytical method: A comparative study," *Energy Convers. Manage.*, vol. 148, pp. 1041–1054, Sep. 2017, doi: [10.1016/j.enconman.2017.06.064](https://doi.org/10.1016/j.enconman.2017.06.064).
- [34] M. Louzazni, A. Khouya, K. Amechnoue, and A. Craciunescu, "Parameter estimation of photovoltaic module using bio-inspired firefly algorithm," in *Proc. Int. Renew. Sustain. Energy Conf. (IRSEC)*, Nov. 2016, pp. 591–596, doi: [10.1109/IRSEC.2016.7983895](https://doi.org/10.1109/IRSEC.2016.7983895).
- [35] A. M. Beigi and A. Maroosi, "Parameter identification for solar cells and module using a hybrid firefly and pattern search algorithms," *Sol. Energy*, vol. 171, no. 1, pp. 435–446, Sep. 2018, doi: [10.1016/j.solener.2018.06.092](https://doi.org/10.1016/j.solener.2018.06.092).